High Precision Dual–Stage Pointing Mechanism for Miniature Satellite Laser Communication Terminals

Riccardo Antonello, *Member, IEEE,* Francesco Branz, Francesco Sansone, Angelo Cenedese *Member, IEEE,* and Alessandro Francesconi

***Abstract*—This paper presents an innovative mechatronic design of a high-accuracy pointing mechanism for orbital laser communication terminals. The system is based on a dual-stage architecture and is miniaturized to fit nanosatellite-class spacecraft, aiming to enable optical communication on small-size space platforms. The focus is on control design aspects and on the performance assessment of an experimental prototype under emulated external environmental disturbances.**

***Index Terms*—Pointing systems, Satellite communication onboard systems, Position control**

I. Introduction

NANOSATELLITES are a class of space vehicles with a total mass ranging between 1 and $10\,\mathrm{kg}$. Originally conceived to offer low cost platforms to ease the access to space of universities, research authorities and small companies, they offer a range of attractive benefits: reduced mass, fast development, minimum launch cost, combined launch of multiple vehicles, improved standardization and modularity. The success of nanosatellites boosted after CubeSats have been proposed in 1999 by California Polytechnic State University and Stanford University [1]. CubeSats are composed by standardized cubic units ($1\,\mathrm{U} = 10\,\mathrm{cm} \times 10\,\mathrm{cm} \times 10\,\mathrm{cm}$, $1.33\,\mathrm{kg}$) and are often released in clusters as piggyback payload of larger missions, or from the International Space Station. Nowadays, a large number of new mission concepts involving miniaturized platforms is constantly proposed. Since the development cost of such platforms is further reduced by mass production, they are typically used in constellations for applications like Earth observation [2] [3], telecommunication [4] [5] and Internet of Things (IoT) [6] [7].

Despite this encouraging background, nanosatellites still present severe technical limitations, especially in terms of limited resources (i.e. power, size, propulsion, attitude control, communication bandwidth, etc.) made available to the payloads, that prevent their use in high performance scientific instrumentation, or viable commercial applications. Profitable scenarios are indeed envisaged, provided that a paradigm shift in current nanosatellites telecom technology (typically VHF, UHF, S or X band communication, with maximum data rates bounded to a few tens of Mbps) is introduced. In this sense, laser communication could lead to a disruptive growth in bit-rate values, with other interesting advantages like link security and the absence of license regulations.

A critical aspect of optical communication is the need for high pointing accuracy. State of the art of small spacecraft attitude control technology is capable to achieve a pointing accuracy below $1.7\,\mathrm{mrad}$, with peak performance as low as $122\,\mu\mathrm{rad}$ [19]. Table I summarizes and compares literature data on the most notable high pointing accuracy systems for small spacecraft. Recently three small-satellite missions have proven high pointing accuracy in the observation of very distant celestial bodies for scientific purposes. The best performances are achieved by the NASA-JPL Arcsecond Space Telescope Enabling Research in Astrophysics (ASTERIA), which is a 6U nanosatellite capable of achieving $2.4\,\mu\mathrm{rad}$ rms of static pointing stability, by exploiting an accurate commercial Attitude Determination and Control Subsystem (ADCS), and a custom fine-pointing piezo stage [8]. Other examples include the $3\,\mathrm{U}$ Miniature X-ray Solar Spectrometer (MinXSS) by University of Colorado Boulder [9], and the BRITE constellation composed of six cubic vehicles [10].

The mentioned missions perform static observations of far objects, while optical communication systems generally deal with dynamic pointing requirements, especially during ground station tracking. Slew rates on $400\,\mathrm{km}$ orbits are typically around $20\,\mathrm{mrad/s}$ [15], greatly stressing the ADCS and making pointing more challenging compared to static observations. In addition, space telescopes platforms are specifically tailored to the pointing task, meaning that the optical payload strongly depends on the vehicle bus resources to achieve such high accuracy. Conversely, satellites integrating a laser communication system are likely to have different primary objectives, thus making impractical or undesired to force the bus to be committed to the pointing task.

The Small Optical TrAnsponder (SOTA) developed by the National Institute of Information and Communications Technology in Japan is one of the first examples of laser communication systems for small satellites; it features a dual stage configuration, with a two-axis gimbal for coarse pointing, and a fine-steering mirror [11]. The NASA Optical Communications and Sensor Demonstration program (OCSD) proves optical

Manuscript received September 26, 2019; revised December 12, 2019; accepted January 22, 2020.

Development of LaserCube Engineering Model has been supported by European Space Agency (ESA)and Italian Space Agency (ASI) in the framework of ESA ARTES C&G Program - Technology Phase (ESA contract no. 4000121651/17/ UK/AD).

Riccardo Antonello, Francesco Branz and Angelo Cenedese are with the Department of Information Engineering, University of Padova, Italy (email: {riccardo.antonello, francesco.branz, angelo.cenedese}@unipd.it).

Alessandro Francesconi is with the Department of Industrial Engineering, University of Padova, Italy (email: alessandro.francesconi@unipd.it).

Francesco Sansone is with Stellar Project s.r.l., Padova, Italy (email: francesco.sansone@stellarproject.space).

TABLE I
HIGH POINTING ACCURACY SYSTEMS ON SMALL SPACECRAFT (SPACE TELESCOPES AND LASERCOM TERMINALS)

	Vehicle volume [cm^3]	**Vehicle mass** [kg]	**System mass** [kg]	**Pointing mode**	**Architecture**	**Accuracy (rms)** [μrad]	**Ref.**
ASTERIA	30 x 20 x 10	10	–	static	FSM	2.4	[8]
MinXSS	30 x 10 x 10	3.5	–	static	body mounted	24	[9]
BRITE	20 x 20 x 20	7	–	static	body mounted	194	[10]
SOTA	50 x 50 x 49	48	5.9	dynamic	gimbal + FSM	19	[11] [12]
OCSD	15 x 10 x 10	2.3	–	dynamic	FSM	140	[13] [14]
NODE	–	–	0.8	dynamic	FSM	16	[15]
OSIRISv3	–	>100	< 5	dynamic	gimbal + FSM	n.a.	[16]
OSIRIS4CubeSat	30 x 10 x 10	–	0.3	dynamic	FSM	n.a.	[16]
Fibertek	–	–	2	dynamic	FSM	20	[17]
CubeCAT	–	–	1.3	dynamic	FSM	n.a.	[18]
LaserCube	–	–	**1.8**	**dynamic**	**parallel platform + FSM**	**< 10**	

NOTE: the mass value is not homogeneous among different systems as it may include a contribution from control electronics and/or telecom hardware.

downlink from two 1.5 U AeroCubes in Low Earth Orbit (LEO) [13], solely relying on the internal ADCS [13], [14]. The MIT Nanosatellite Optical Downlink Experiment (NODE) instead integrates a Fast Steering Mirror (FSM) in a 1.2 U to improve the pointing accuracy achieved with the ADCS [20], [15]. NODE will be the payload of the Cubesat Laser Infrared CrosslinK (CLICK) mission which is under joint development by MIT, University of Florida and NASA Ames Research Center [21]. The Optical Space Infrared Downlink System (OSIRIS) program of the German Aerospace Center (DLR) is currently testing different optical communication terminals for a wide range of satellites, from small satellites (OSIRISv3) to CubeSat-compatible (OSIRIS4CubeSat) sizes. The latter will be possibly deployed to space in the near future, on board of a 3 U platform [16].

Most of the aforementioned systems heavily rely on the spacecraft capabilities for coarse pointing, thus limiting the operational flexibility of the mission. Instead, great advantages for optical communication are expected if few or no architectural modifications to the orbital platform are required. For this reason, Stellar Project (a spin-off of the University of Padova, Italy) has been developing LaserCube, a lasercom terminal for CubeSats based on an innovative dual-stage pointing system, featuring a parallel platform mechanism for coarse pointing, and a steering mirror mounted above it for fine adjustments. Compared to other dual-stage designs, such as those exploited in SOTA and OSIRISv3 terminals, both consisting of steering mirrors mounted on gimbal suspensions, the LaserCube system is more compact (the opto-mechanical unit fits in 1 CubeSat unit), thus allowing an easy integration on CubeSat platforms without the need for protrusions (as in OSIRISv3).

This paper describes the LaserCube pointing control system, with focus on design aspects and laboratory validation under specific disturbances.

II. THE LASERCUBE COMMUNICATION TERMINAL

A. LaserCube architecture

LaserCube is composed by four main subsystems: the Miniature Optical Subsystem (MOS), the Miniature Pointing and Stabilization Subsystem (MPSS), the Miniature Telecom Subsystem (MTS) and the Payload Electronic Board (PEB). The MPSS and MOS compose the opto-mechanical unit of LaserCube. The MTS and PEB form the LaserCube Electronic Unit. The MOS emits the transmitting laser beam with controlled divergence, and collects the incoming light from the remote terminal on an Optical Sensor (OS), enabling the measurement of the misalignment between LaserCube and the communication direction. The MTS is the electronic package required for modulation and demodulation of optical signals. The MPSS is the pointing mechanism that aligns the MOS optical axis with the incoming beam. It is based on a dual-stage configuration, which is schematically depicted in Fig. 1.

The first stage is a parallel platform with two rotational degrees-of-freedom (DoFs), used to perform coarse pointing (range $\pm 10\,\mathrm{deg}$, accuracy $50\,\mu\mathrm{rad}$ rms). Actuation is provided by two linear walking piezo-motors. The mechanical design is protected by an international patent [22]. The second stage is a Fast Steering Mirror (FSM), moved by a dual-axis tip-tilt piezo-stage, that deflects the incoming laser beam on the OS. It is used to achieve fine pointing (range $\pm 0.7\,\mathrm{mrad}$, accuracy $<10\,\mu\mathrm{rad}$ rms). Additional details are provided in Sec. V-A.

B. Operational scenarios

LaserCube is conceived to support optical communication in both downlink (DL) and intersatellite-link (ISL) applications. Orbital considerations determine the mechanism requirements in terms of maximum rotation angle and slewing rate. In the DL case, the system transmits spaceborne data towards an optical ground station during the visibility time window. Expected orbital parameters allow to estimate a link availability in the order of $400\,\mathrm{s}$, considering a minimum elevation angle

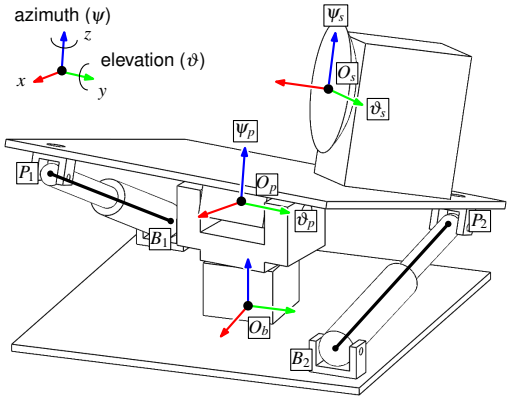

Fig. 1. Simplified MPSS kinematic model (3D view). The frames with origins O_b, O_p, O_s are related to, respectively, the LC base, the parallel platform (primary stage), and the fast steering mirror (secondary stage).

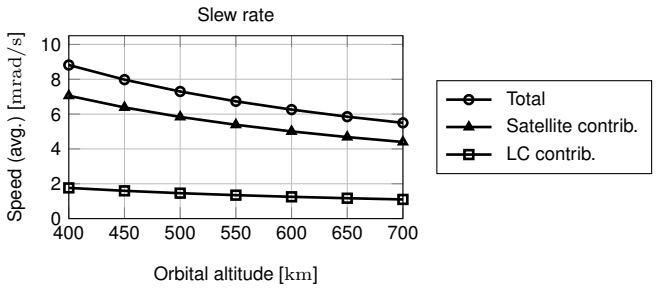

Fig. 2. Typical slew rate required to track a ground station from LEO, as a function of orbit altitude, with orbit inclination equal to $90\,\mathrm{deg}$ (*circles*: total slew rate; *triangles* and *squares*: slew rate allocation between satellite and LaserCube).

over the horizon of $15\,\mathrm{deg}$. During this period, a slewing maneuver is executed in cooperation between the satellite and the LaserCube coarse pointing system: the satellite rotates in order to point towards the ground station with a maximum pointing error of $20\,\mathrm{deg}$ on the whole pass, while LaserCube aligns itself towards the ground station and compensates for the pointing error of the satellite. In this situation, the satellite shall perform a manoeuvre close to $150\,\mathrm{deg}$ ($\pm 75\,\mathrm{deg}$) with an average slewing rate between 4 and $8\,\mathrm{mrad/s}$, while LaserCube performs a $20\,\mathrm{deg}$ ($\pm 10\,\mathrm{deg}$) rotation with a slewing rate between 1 and $2\,\mathrm{mrad/s}$, as shown in Fig. 2.

In ISL scenarios, the system is instead used to relay data between satellites placed in the same orbital plane. Nominally, in circular orbits the relative dynamic is null; in practice, non-ideal orbital positions and perturbations result in variations of the line of sight connecting the two satellites. Such variability can sum up to $\pm 4\,\mathrm{deg}$, with the main motion harmonic related to the orbital period (around $90\,\mathrm{min}$ at 500–700 km of altitude). Relative angular velocity is on the order of $80\,\mu\mathrm{rad/s}$.

Differently, the design requirements in terms of pointing accuracy come from the link budget, as a function of laser beam divergence. In ISL mode, LaserCube is designed to guarantee $100\,\mathrm{Mbps}$ with a $1000\,\mathrm{km}$ baseline, or $10\,\mathrm{Mbps}$ at $2000\,\mathrm{km}$. In such conditions the beam divergence is $50\,\mu\mathrm{rad}$. In order to minimize pointing losses, the pointing requirement becomes $\pm 10\,\mu\mathrm{rad}$ rms.

Regardless of the communication link mode, the pointing performance has to be achieved in a disturbed environment. The main perturbations come from the bus oscillations (attitude jitter) due to attitude control limitations, and from micro-vibrations caused by the operation of moving parts.

III. MPSS Modeling

A. Kinematic model

The simplified kinematic configuration of the MPSS is shown in Fig. 1. The primary stage mechanism contains two spherical joints (the linear motors top joints P_1 and P_2), three joints with two DoFs (the platform central joint O_p and the bottom-joints B_1 and B_2 of the legs) and two prismatic joints (the segments $\overline{B_1P_1}$ and $\overline{B_2P_2}$, representing the two linear actuators). The kinematic configuration allows the platform to rotate around the y and z axes of the platform–fixed reference frame, but not around the x–axis. Similarly, the FSM can be reoriented around the y and z axes of its own reference frame. The vectors $\boldsymbol{\phi}_p = [\vartheta_p,\, \psi_p]^T$ and $\boldsymbol{\phi}_s = [\vartheta_s,\, \psi_s]^T$ are used to denote the attitude of, respectively, the platform with respect to the base, and the FSM with respect to the platform. The vectors $\boldsymbol{\phi}_e = [\vartheta_e,\, \psi_e]^T$ and $\boldsymbol{\phi}_l = [\vartheta_l,\, \psi_l]^T$ are instead introduced to describe the orientation of the laser beam reference frame with respect to, respectively, the FSM and base reference frames. The vector $\boldsymbol{\phi}_e$ is indeed the attitude measurement provided by the OS, which is indeed the attitude error of the FSM frame with respect to the incident laser beam direction. In general it holds that

$$\boldsymbol{R}_l^s(\boldsymbol{\phi}_e) \;=\; [\boldsymbol{R}_s^p(\boldsymbol{\phi}_s)]^T [\boldsymbol{R}_p^b(\boldsymbol{\phi}_p)]^T \boldsymbol{R}_l^b(\boldsymbol{\phi}_l) \tag{1}$$

where $\boldsymbol{R}_b^a(\boldsymbol{\phi})$ denotes the rotation matrix of the generic reference frame $\mathcal{F}_b$ with respect to $\mathcal{F}_a$, with $\boldsymbol{\phi}$ the relative orientation vector; by adopting a ZYX Euler angle sequence to express rotations, it follows that $\boldsymbol{R}_b^a(\boldsymbol{\phi}) = \boldsymbol{R}_z(\psi)\, \boldsymbol{R}_y(\vartheta)$, where $\boldsymbol{R}_z$ and $\boldsymbol{R}_y$ are the generic rotation matrices with respect to the z and y axes, respectively. However, for a small orientation error, the trigonometric identity (1) reduces to:

$$\boldsymbol{\phi}_e \;\approx\; \boldsymbol{\phi}_l - \boldsymbol{\phi}_p - \boldsymbol{\phi}_s \tag{2}$$

This approximated algebraic relation is adopted throughout the paper to define MPSS pointing error, on which both the model of the dual–stage actuation mechanism, and the related attitude control system rely.

The kinematic model of the primary stage consists of the following set of two trigonometric equations:

$$G_i(\boldsymbol{\phi}_p, \boldsymbol{l}) \triangleq \|\overrightarrow{O_bB_i} + \overrightarrow{O_bO_p} + \overrightarrow{P_iO_p}\|^2 - l_i^2 = 0 \tag{3}$$

where $l_i = \|\overrightarrow{B_iP_i}\|$ is the length of the i-th linear motor shaft ($i = 1, 2$). The model defines, in implicit form, a relationship between the lengths $\boldsymbol{l} = [l_1,\, l_2]^T$ of the two motor shafts, and the platform orientation $\boldsymbol{\phi}_p$. For a mechanism with a parallel kinematics such as the MPSS, only the former has a closed-form expression; the latter, instead, has to be determined with numerically methods [23], [24].

B. Simplified dynamic model

A simplified dynamical model of the MPSS is obtained under the assumption that the accelerations experienced by the mechanism during normal operation are sufficiently small. In this way, all the dynamic contributions due to the moving masses can be neglected, and the motion can be described by simply resorting to the kinematic model derived in Sec. III-A. By accounting for the dynamics of the servo-drives used to control the MPSS actuators, the following simplified dynamic model is obtained for the primary stage:

$$\boldsymbol{\phi}_p = \boldsymbol{g}_{dkin}(\boldsymbol{l}) \qquad \text{with} \qquad \boldsymbol{l} = \boldsymbol{G}_p(s)\, \boldsymbol{l}^* \tag{4}$$

where $\boldsymbol{G}_p(s)$ is a 2×2 diagonal transfer matrix whose elements on the leading diagonal are the transfer functions of the two linear motors servo–drives, and $\boldsymbol{l}^*$ the position references provided to them. Even though the diagonal elements of the transfer matrix can be in general different to account for possible mismatches in the two servo–drives responses, in the following they are assumed identical, and denoted with $G_p(s)$. As for the secondary stage, assuming that the two angles are directly controlled by the stage servo–drive, it holds that:

$$\boldsymbol{\phi}_s = \boldsymbol{G}_s(s)\, \boldsymbol{\phi}_s^* \tag{5}$$

where $\boldsymbol{G}_s(s)$ is a 2×2 diagonal transfer matrix (provided that the axis coupling is negligible), whose elements on the leading diagonal are the transfer functions of the two servo–actuated axes, and $\boldsymbol{\phi}_s^*$ the angle references provided to the servo–drive. Similarly to the primary stage, the diagonal elements of the transfer matrix are assumed identical, and denoted with $G_s(s)$.

IV. Control System Design

A. Control architecture

The MPSS pointing control system has two different modes of operations, namely the laser beam *seeking* and *tracking modes*, which are managed by two different ad-hoc controllers. While in seeking mode, the MPSS platform is moved to scan the whole operational space, in search for an incoming laser beam. When the laser beacon is detected by the OS, the controller switches to the tracking mode, whose aim is to keep the laser spot at the center of the sensor field-of-view (FOV), by continuously adjusting the orientations of the two stages. The seeking–to–tracking controller switching has to be properly managed to avoid abrupt command variations that potentially cause the laser beacon loss (*bumpless transfer*).

The design of the beam–seeking controller does not pose particular challenges, because it only requires to drive the two MPSS linear motors with suitable position reference commands. On the other hand, the design of the beam–tracking controller is more challenging, since it requires to properly coordinate the dual–stage actuation system in order to meet the required pointing accuracy. The design details are reported in the next section.

B. Beam-tracking control design

The design of the MPSS dual-stage beam-tracking controller is based on the *sensitivity decoupled method* proposed in [25], [26]. The method enables a separate design for the controllers of the primary and secondary stage, while guaranteeing that the sensitivity of the resulting dual–stage control system is the product of the sensitivities of the two independent designs. The control structure is given in Fig. 3.

The primary-stage controller $\boldsymbol{C}_p(z)$ is designed by exploiting a kinematic inversion principle. The controller computes the platform orientation reference $\boldsymbol{\phi}_p^*$ by using the orientation

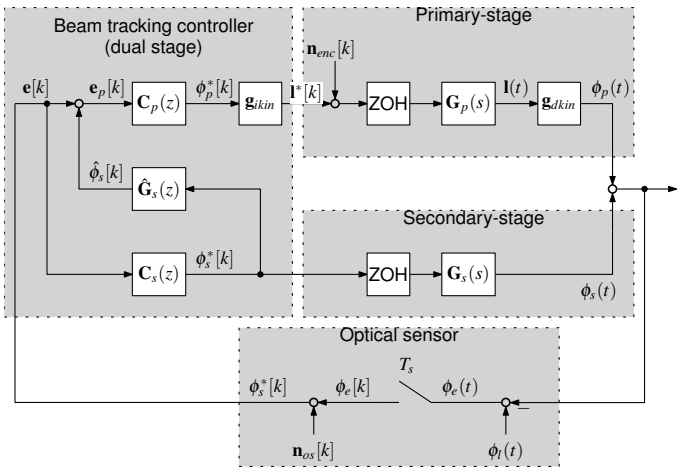

Fig. 3. MPSS dual-stage beam-tracking control system: overall architecture.

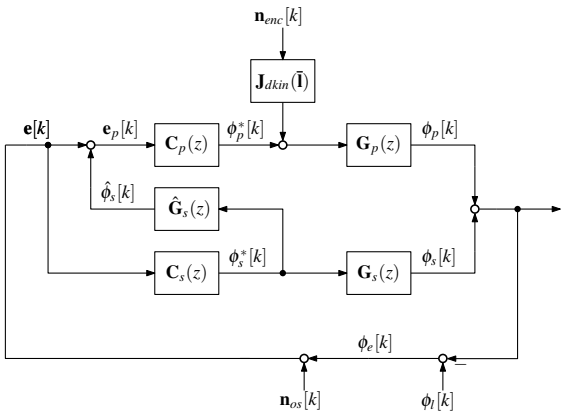

Fig. 4. MPSS dual-stage beam-tracking control system: linearized model.

error feedback $\boldsymbol{\phi}_e$ provided by the optical sensor. The position references $\boldsymbol{l}^*$ for the two linear motor servo-drives are then obtained with the inverse kinematics function $\boldsymbol{g}_{ikin}$ of the primary-stage. The control design is performed by linearizing the kinematic functions in the block diagram of Fig. 3 around a certain working point $(\bar{\boldsymbol{\phi}}_p, \bar{\boldsymbol{l}})$. Their linearizations correspond to the Jacobian matrices:

$$\boldsymbol{J}_{dkin}(\bar{\boldsymbol{l}}) = \frac{\partial \boldsymbol{g}_{dkin}(\bar{\boldsymbol{l}})}{\partial \boldsymbol{l}}\,, \quad \boldsymbol{J}_{ikin}(\bar{\boldsymbol{\phi}}_p) = \frac{\partial \boldsymbol{g}_{ikin}(\bar{\boldsymbol{\phi}}_p)}{\partial \boldsymbol{\phi}_p} \tag{6}$$

The linearized model from the control command $\boldsymbol{\phi}_p^*$ to the platform attitude $\boldsymbol{\phi}_p$ is therefore equal to:

$$\begin{aligned} \boldsymbol{J}_{dkin}(\bar{\boldsymbol{l}})\,\boldsymbol{G}_p(s)\,\boldsymbol{J}_{ikin}(\bar{\boldsymbol{\phi}}_p) \;&=\; \cdots \\ \cdots \boldsymbol{G}_p(s)\,\boldsymbol{J}_{dkin}(\bar{\boldsymbol{l}})\,\boldsymbol{J}_{ikin}(\bar{\boldsymbol{\phi}}_p) \;&=\; \boldsymbol{G}_p(s) \end{aligned} \tag{7}$$

where the first identity holds because $\boldsymbol{G}_p(s)$ is a diagonal matrix, while the latter exploits the property of the two Jacobians to be one the inverse of the other. Since the resulting transfer matrix is diagonal, the controllers for the elevation and azimuth angles are fully decoupled (no off-diagonal elements required in $\boldsymbol{C}_p(z)$), and they can be independently designed. In practice, unless otherwise required, the same design applies for both axes, because the closed-loop transfer functions of the two motor servo-drives are assumed identical. A PID structure is selected for the two controllers; the design is performed to meet the desired levels of tracking accuracy and noise/disturbance rejection (see Sec. IV-D).

Thanks to the sensitivity decoupled method, the secondary-stage controller $\boldsymbol{C}_s(z)$ can be designed as an "add-on" component for the primary one. Similarly to the primary-stage, the controllers of the two secondary-stage axes are decoupled and identically designed (provided that $\boldsymbol{G}_p(s)$ is diagonal, with identical elements on the leading diagonal). A model $\hat{\boldsymbol{G}}_s(z)$ of the FSM input–output dynamics is used as an open–loop observer to estimate the FSM orientation, which is in general not detectable. The FSM orientation estimate $\hat{\boldsymbol{\phi}}_s$ can be obviously replaced with its measurement $\boldsymbol{\phi}_s$ whenever an ad–hoc sensor is available on the FSM to sense such quantity. For the design of the dual–stage controller, consider the linearized version of the block diagram in Fig. 3, reported in Fig. 4. In the block diagram, the transfer matrices of the primary and secondary stages servo-drives have been discretized with the exact discretization method [27]. The control system consists

of two identical and independent tracking control loops, since both the controller and plant (MPSS primary/secondary–stage) transfer matrices are diagonal, with identical entries on the leading diagonal. Therefore, the control design can be carried out for a single tracking loop, by considering scalar quantities. The sensitivity transfer function of a single loop is:

$$S(z) \;=\; \frac{e(z)}{\phi_l(z)} \;=\; S_p(z)\,\hat{S}_s(z) \tag{8}$$

where

$$S_p(z) = \frac{1}{1 \,+\, C_p(z)\,G_p(z)} \tag{9}$$

$$\hat{S}_s(z) = \frac{1}{1 \,+\, K(z)\,C_s(z)\,G_s(z)} \tag{10}$$

with

$$K(z) \;=\; \frac{1 \,+\, C_s(z)\,\hat{G}_s(z)}{1 \,+\, C_s(z)\,G_s(z)} \tag{11}$$

In the previous equations, e and ϕ_l denote, indifferently, the first or second component of the vectors $\boldsymbol{e}$ and $\boldsymbol{\phi}_l$; the transfer functions $C_p(z)$, $C_s(z)$, $G_p(z)$, $G_s(z)$ and $\hat{G}_s(z)$ are the diagonal entries of the corresponding transfer matrices.

It is immediate to notice that (9) is the sensitivity of the primary–stage control loop, while (10) is an approximation of that of the secondary–stage, which coincides with the actual one when the coupling factor $K(z)$ is unitary. In practice this situation occurs when $G_s(z) = \hat{G}_s(z)$ (i.e. when the secondary-stage model is perfect or, alternatively, when the secondary-stage attitude is directly measured with an ad-hoc sensor), or even in case when $G_s(z) \neq \hat{G}_s(z)$, provided that the model mismatch occurs on a frequency range where the attenuation introduced by the controller $C_s(z)$ is sufficiently high. Therefore, the identity (8) suggests that when $K(z) \approx 1$, the dual–stage control design can be decoupled into two independent control designs for the primary and secondary–stage loops.

Similarly to the primary-stage, conventional PID controllers are used for the secondary-stage; their design is aimed to boost the low-frequency attenuation of the primary-stage sensitivity function, in order to meet the desired levels of tracking accuracy and disturbance/noise attenuation.

C. Integrator anti-windup architecture for primary-stage

Proper integrator anti-windup schemes must be implemented on the primary and secondary stages, to avoid the unnecessary accumulation of the tracking error in the PID integrators during large positioning transients. A conventional scheme can be adopted for the secondary-stage [28]; on the other hand, the primary-stage requires some modifications, since the actuation limits must be detected in the joint-space (i.e. elongation of linear motor shafts), rather than in the operational-space (i.e. platform orientation angles) where the PID controller operates. The proposed implementation for the primary-stage is shown in Fig. 5. It works by comparing the "unsaturated" outputs $\boldsymbol{\phi}_p^*$ of the two PID controllers with the platform orientation $\boldsymbol{\phi}_{p,sat}^*$ that complies with the actuators limits. These are obtained by applying to the "unsaturated" motors servo–drives commands $\boldsymbol{l}^*$, computed by kinematics inversion, the same limits experienced by the real actuators,

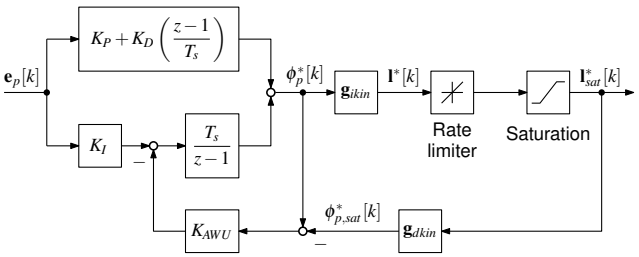

Fig. 5. Integrator anti-windup scheme for primary-stage. The PID controller is implemented in parallel-form; the integral and derivative terms are discretized with the Forward Euler method.

in terms of maximum stroke and rate–of–change. Then, the "saturated" commands $\boldsymbol{l}_{sat}^*$ are converted back, through the direct kinematics, to a platform orientation compatible with the actuators limits. The difference between the "unsaturated" and "saturated" commands is used as a compensation signal that keeps the inputs of the two PID integrators as small as possible when the actuators saturates.

D. Error Budgeting

The linearized model of the beam-tracking control system obtained in Sec. IV-B allows to readily assess what is the contribution of each noise source to the overall tracking error (*error budget analysis*), without resorting to extensive simulation campaigns. With the aid of this analysis, the beam-tracking PID controllers are then designed to meet the required tracking accuracy specification, typically by shaping the overall sensitivity function to obtain the necessary noise attenuation level. The main noise sources, as also indicated in the block diagram of Fig. 3, are the encoders quantization noise $\boldsymbol{n}_{enc}$ of the two linear motors (the underlying assumption here is that the positioning accuracy of the two linear motor servo-drives is never lower than the resolution of the two encoders), the output noise $\boldsymbol{n}_{os}$ of the optical sensor, and the jitter motion of the satellite bus, that can be represented as a disturbance $\boldsymbol{n}_{jit}$ superimposed to the beam orientation reference $\boldsymbol{\phi}_l$.

With reference to a single orientation axis (indifferently elevation or azimuth – according to the assumptions made in Sec. IV-B, the dynamic responses of the two axes are identical), the contribution $\sigma_{e_i}^2$ of the i^{th} noise source to the overall tracking error variance σ_e^2 can be evaluated as

$$\sigma_{e_i}^2 = \frac{1}{2\pi F_s}\int_0^{2\pi F_s} |H_i(e^{j\omega T_s})|^2\, P_{n_i}(\omega)\, d\omega \tag{12}$$

where $H_i(z)$ is the transfer function from the noise source n_i to the tracking error e, $P_{n_i}(\omega)$ is the power spectral density of the noise source, and $F_s = 1/T_s$ is the sampling frequency. Thanks to the statistical independence of the different noise sources, the overall tracking error variance is obtained as the sum of the different contributions. It can be easily verified that

$$H_{enc}(z) = G_p(z)\,S(z)\,, \quad H_{os}(z) = H_{jit}(z) = S(z) \tag{13}$$

Both the encoders quantization and the optical sensor measurement errors can be considered as white noises with variances $\sigma_{enc}^2 = q_{enc}^2/12$ and σ_{os}^2, with q_{enc} being the encoder quantization step. The satellite bus jitter is instead a noise with spectrum envelope as shown in Fig. 6. The profile is representative of 6 U CubeSat satellite in LEO, equipped

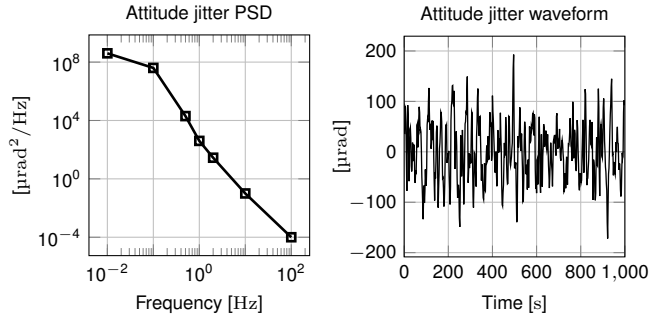

(a) (b)

Fig. 6. Satellite attitude jitter for a 6 U CubeSat in LEO, equipped with medium/high performance ADCS: (a) spectrum envelope; (b) typical waveform.

with medium/high performance ADCS. The jitter noise can be generated as the output of a noise-shaping filter with frequency response as shown in Fig. 6a, driven by a white noise with variance equal to T_s. Data are inferred from attitude control simulations of a $10\,\mathrm{kg}$ satellite in LEO [29] [30]. The simulations do not take into account potential disturbances induced by the LaserCube moving parts on the satellite attitude control system. However, being the moving mass of the MOS at least one order of magnitude smaller than the minimum satellite mass, and the accelerations imposed to the mechanism rather small, it is expected that their effects are similar to those produced by the typical environmental disturbances affecting the motion of small satellites in low Earth orbit.

A final contribution to the total error budget is the intrinsic error of the feedback controller in following non–constant attitude reference input ϕ_l. For a sinusoidal reference with amplitude A and angular frequency ω, it holds that the steady-state tracking error is again a sinusoidal signal with amplitude $A_e = A\left|S(e^{j\omega T_s})\right|$, which contributes to the total error variance by an amount equal to the signal power, namely $\sigma_e^2 = A_e^2/2$.

V. Experimental Results

A. Experimental testbed

A complete engineering model (EM) of the LaserCube MPSS has been developed for experimental testing, by using off–the–shelf components. A photo of the EM is shown in Fig. 7a with external dimensions and optical aperture size. The primary-stage actuators are linear walking piezo-motors with embedded optical sensors (stall force $6.5\,\mathrm{N}$, position resolution $<1\,\mathrm{nm}$), controlled in closed-loop with their own miniature drivers. The secondary-stage is instead actuated by a dual-axis tip-tilt piezo-stage, controlled in open-loop with its own servo-controller. The piezo-stage includes strain gauges for position sensing (used in the beam-tracking implementation described in Sec. IV-B). The OS is a photodiode-based quadrant-detector ($12\,\mathrm{mm}^2$ active area per element).

The EM is controlled by a PEB prototype, whose simplified functional diagram is shown in Fig. 7b. Despite not being the final flight version, it implements all the functions required to correctly operate the LaserCube system. It is centered around an ARM Cortex-M4 micro-controller unit (MCU).

For testing the capability of the MPSS to reject undesired motions of its base (e.g. jitter motion of the satellite bus), the EM has been installed on top of a motorized pan-tilt stage unit, comprising two stepper motors with reduction gears. The stage has been controlled with a custom board, which generates the desired motion profiles for the two motors.

B. Control system implementation

The beam-tracking PID controllers have been designed in continuous-time with conventional frequency domain methods, using the servo-drives models obtained with ad-hoc system identification experiments. The Bode plots of the identified models are shown in Fig. 8. The model of the primary-stage servo-drive consists of a first-order low-pass system with cut-off frequency equal to $0.26\,\mathrm{Hz}$, plus a time-delay of $2.5\,\mathrm{ms}$. As for the secondary-stage, the model is a constant gain equal to 0.63, plus a time-delay of $5\,\mathrm{ms}$.

The design parameters have been selected to obtain a tracking error standard deviation, as predicted by the error budget analysis of Sec. IV-D, within the required specification ($\pm 10\,\mu\mathrm{rad}$ rms). With a gain crossover frequency ω_{gc} equal to $2.6\,\mathrm{Hz}$ for the primary stage, and $30\,\mathrm{Hz}$ for the secondary, a phase margin φ_m of $75\,\mathrm{deg}$ for both stages, and a sampling period equal to $T_s = 1\,\mathrm{ms}$, the error budget is as reported in Tab. II. The budget is obtained with a standard deviation $\sigma_{os} = 0.21\,\mu\mathrm{rad}$ for the OS, that accounts for both the intrinsic sensor output noise and the ADC quantization, and $\sigma_{enc} = 0.36\,\mu\mathrm{rad}$ for the encoder quantization of the linear motors. The sinusoidal references used for the ISL and DL scenarios are rescaled versions of the actual ones, with amplitude of $0.1\,\mathrm{deg}$ and frequencies equal to $0.025\,\mathrm{Hz}$ for the ISL case, and $0.5\,\mathrm{Hz}$ for the DL case (see Sec. V-C for the rescaling details).

Unfortunately, a $1\,\mathrm{ms}$ sampling period is incompatible with the bandwidth limitation imposed by the serial TTL communication interface between the MCU and primary-stage servo-drives. In order to comply with this limitation, without sacrificing the tracking performances of the overall system, a *dual-rate* implementation has been adopted, with sampling periods equal to $T_{s,1} = 10\,\mathrm{ms}$ for the primary stage, and $T_{s,2} = 1\,\mathrm{ms}$ for the secondary stage. The expected performances of the dual-rate implementation are somehow in between the performances obtained with a single-rate scheme operating either at the fast or slow rate. A more accurate prediction can be obtained by adapting the analysis of Sec. IV-D to the case of a dual-rate system, by using conventional lifting techniques for multi-rate systems [31].

The control system has been designed, developed and tested directly in the MATLAB/Simulink environment, by following a rapid control prototyping (RCP) methodology. Extensive customization has been required to access the dedicated hardware

TABLE II
Tracking Error Budget Analysis

Contribution	**Elevation** [μrad]	**Azimuth** [μrad]
Linear motors encoders	0.1898	0.0560
Optical sensor	0.3855	0.3855
Attitude jitter (med-perf ADCS)	2.9967	2.9967
Sinusoidal ref (ISL scenario)	0.0034	0.0034
Sinusoidal ref (DL scenario)	2.7220	2.7220
Total (ISL scenario)	3.0243	3.0216
Total (DL scenario)	4.5430	4.0669

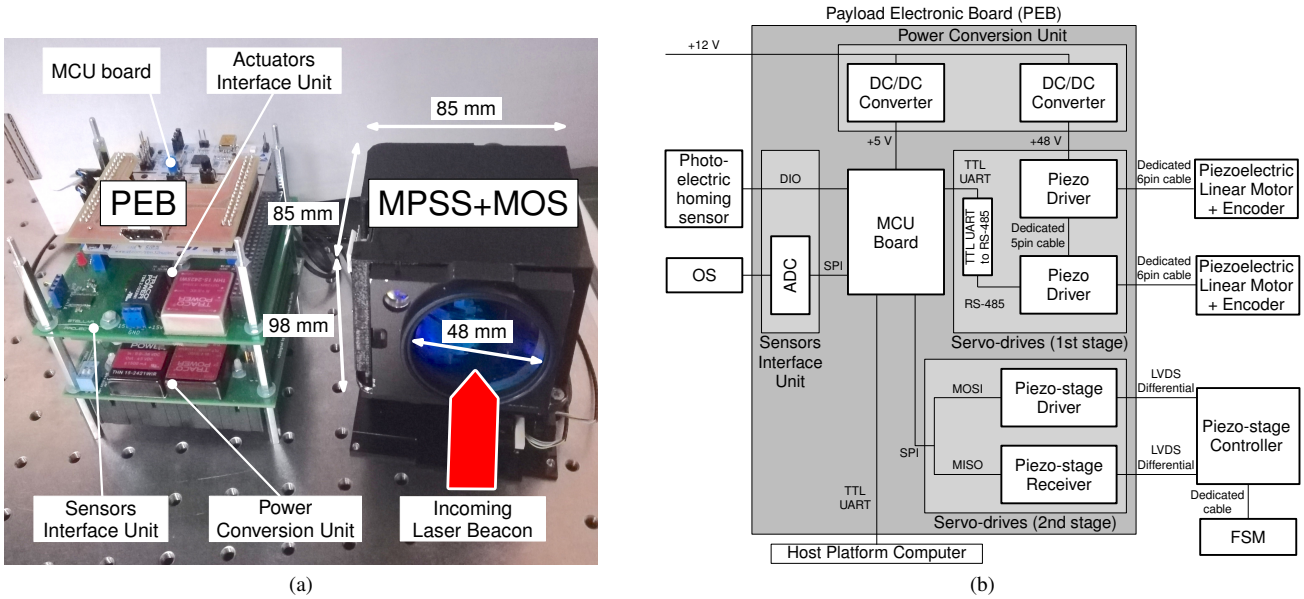

Fig. 7. Experimental testbed: (a) LaserCube opto-mechanical EM unit; (b) functional diagram of PEB prototype.

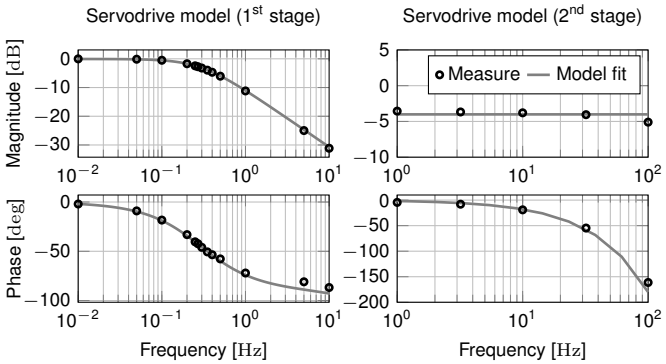

Fig. 8. Servodrive model identification: primary-stage (left); secondary-stage (right).

and peripherals, and to schedule the primary and secondary-stage control tasks without resorting to any real-time operating system (*bare-metal* implementation). The direct and inverse kinematic functions used in the primary-stage control loop are implemented as two 32×32 look-up tables (LUT), with breakpoints equally spaced in their respective domains. The linear-motors stroke and speed limits required to implement the anti-windup scheme of Sec. IV-C are retrieved from manufacturer's data-sheets.

TABLE III
TRACKING ACCURACY TEST RESULTS

Imposed trajectory$^{(*)}$		Tracking error std (elevation direction)		Tracking error std (azimuth direction)	
Freq. [Hz]	**Peak vel.** [mrad/s]	**Elevation** [μrad]	**Azimuth** [μrad]	**Elevation** [μrad]	**Azimuth** [μrad]
0.025	0.27	1.13	1.23	0.64	2.05
0.05	0.55	0.94	0.83	0.74	1.11
0.1	1.10	1.24	0.93	1.00	1.76
0.2	2.19	2.43	1.64	2.35	2.06
0.5	5.48	6.77	4.11	5.33	6.63

$(*)$ Trajectory amplitude equal to $1.75\,\mathrm{mrad}$

C. Tracking accuracy test

The aim of this test is to verify the LaserCube capability to track motion patterns similar to those experienced by the system during ISL and DL modes. It is performed by mounting and aligning the EM and the laser beacon on a vibration-isolated optical table, and by imposing predefined reference trajectories to the MPSS attitude controller. The OS readout is used as a measure of the misalignment error between the MOS optical axis and the incoming laser beam direction. The reference trajectories are estimated from orbit considerations: a low frequency ($0.17\,\mathrm{mHz}$) oscillation with $70\,\mathrm{mrad}$ amplitude is considered realistic for the ISL scenario ($80\,\mu\mathrm{rad/s}$ maximum angular velocity); for the DL scenario, a linear rotation with quasi-constant velocity around $1\,\mathrm{mrad/s}$ is envisaged. Unfortunately, these profiles exceed the limited OS range, and cannot be directly used for testing. To overcome this limitation, tests are performed by down-scaling the amplitude of the reference trajectories, while simultaneously increasing their frequency to preserve the imposed maximum angular velocity. In addition, the sinusoidal motion is considered more demanding compared to the linear motion, thus the DL tracking capability is also verified with a sinusoidal trajectory.

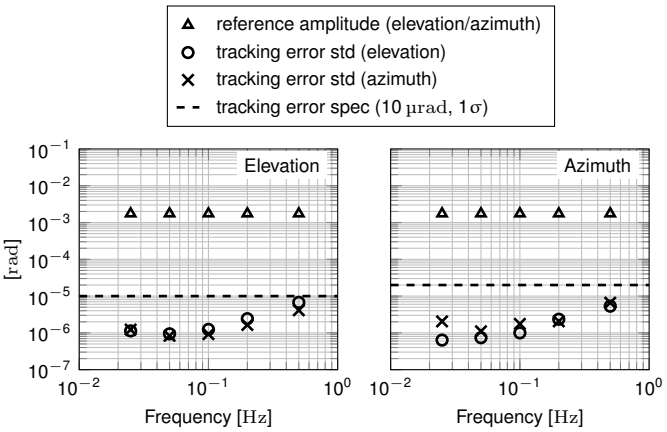

Fig. 9. MPSS tracking accuracy tests: sinusoidal reference on elevation direction (left); sinusoidal reference on azimuth direction (right).

Table III summarizes the test results in terms of overall tracking errors in various conditions. The peak target velocities during tests vary over a wide dynamic range around those estimated for realistic scenarios. Note that the tracking error standard deviation is always well below the required $10\,\mu\mathrm{rad}$ accuracy level. The same results are graphically summarized in Fig. 9.

D. Disturbance rejection test

The aim of this test is to assess the MPSS rejection capabilities to residual attitude jitter of the satellite bus. It is performed by mounting the LaserCube EM on top of a pan–tilt stage unit (see Sec. V-A), installed on top of a vibration-isolated optical table. A laser beam source is also fixed to the table and aligned with the MOS. The misalignment error between the MOS optical axis and the fixed laser direction is tracked with the OS, while the pan-tilt stage is simultaneously moved to emulate a realistic jitter motion of the host satellite.

Test results are summarized in Tab. IV, and graphically shown in Fig. 10. The disturbance motion parameters imposed to the MPSS base are chosen following the considerations detailed in Sec. II-B, leading to frequencies ranging from 0.01 to $10\,\mathrm{Hz}$ and corresponding amplitudes decreasing from 17 to $0.05\,\mathrm{mrad}$. The selected disturbances always have an amplitude larger or equal to the satellite attitude jitter envelope presented in Fig. 6a and rescaled in Fig. 10 for reference. Note that the standard deviation of the overall pointing error is generally below $10\,\mu\mathrm{rad}$ for the considered range of disturbances.

TABLE IV
DISTURBANCE REJECTION TEST RESULTS

Imposed disturbance		**Pointing error std (tilt motion)**		**Pointing error std (pan motion)**	
Freq. [Hz]	**Ampl.** [mrad]	**Elevation** [μrad]	**Azimuth** [μrad]	**Elevation** [μrad]	**Azimuth** [μrad]
0.01	17	6.81	1.72	2.65	4.76
0.02	8.5	6.76	1.83	2.65	4.95
0.04	2	3.43	1.45	2.28	4.20
0.1	2	7.05	1.67	2.46	4.90
0.2	0.8	6.97	1.78	2.49	4.34
0.3	0.4	6.13	1.56	1.73	3.29
0.5	0.2	4.50	1.58	2.22	4.16
1	0.05	1.03	0.88	1.92	3.97
3	0.05	1.15	1.12	1.54	3.68
10	0.05	11.47	1.66	1.34	5.24

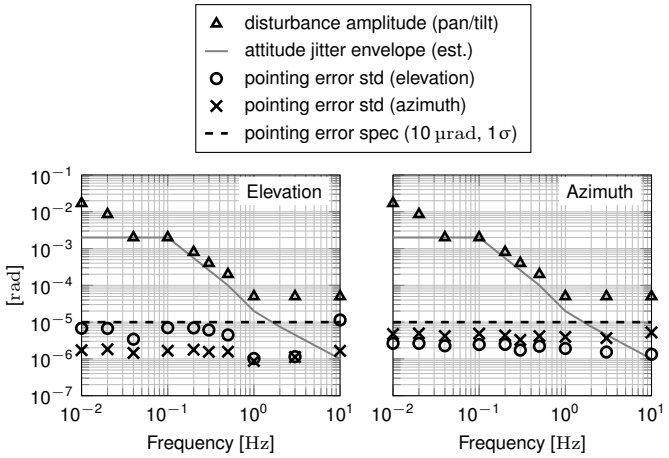

Fig. 10. MPSS disturbance rejection tests: sinusoidal disturbance on elevation direction (left); sinusoidal reference on azimuth direction (right).

VI. Conclusions

A novel mechatronic design of a high-accuracy, miniature pointing mechanism for orbital laser communication terminals has been proposed. The device is compatible with CubeSat-class vehicles, thus effectively enabling high-bandwidth and secure data communication in constellations of nanosatellites. High pointing accuracy is attained with a dual-stage positioning mechanism comprising a parallel platform for coarse motions, and a fast-steering mirror for fine adjustments. The system weights $1.8\,\mathrm{kg}$, and fits within a $2\,\mathrm{U}$ envelope ($20\,\mathrm{cm} \times 10\,\mathrm{cm} \times 10\,\mathrm{cm}$). A control system capable of coordinating the motion of the two stages for achieving the desired pointing accuracy has been designed and validated with thorough experimental testing performed on a full-scale engineering model of the mechanism. Results show that the proposed solution is indeed capable of satisfying the required control specifications, with pointing error below $10\,\mu\mathrm{rad}$ std (optical angle) in both trajectory tracking and disturbance rejection tests.

References

[1] California Polytechnic State University. CubeSat Design Specifications. [Online]. Available: https://static1.squarespace.com/static/5418c831e4b0fa4ecac1bacd/t/56e9b62337013b6c063a655a/1458157095454/cds_rev13_final2.pdf
[2] Planet Labs. [Online]. Available: https://www.planet.com/company/approach/
[3] Aquila Space. [Online]. Available: http://www.aquilaspace.com/landmapper/
[4] Analytical Space. [Online]. Available: https://www.analyticalspace.com/
[5] Sky and Space Global. [Online]. Available: https://www.skyandspace.global/operations-overview/technology/
[6] Astrocast. [Online]. Available: https://www.astrocast.com/
[7] Aistech Space. [Online]. Available: https://www.aistechspace.com/
[8] M. W. Smith *et al.*, "On-orbit results and lessons learned from the ASTERIA space telescope mission," in *32nd Annual AIAA/USU Conference on Small Satellites*, 2018.
[9] J. P. Mason *et al.*, "MinXSS-1 CubeSat on-orbit pointing and power performance: The first flight of the Blue Canyon Technologies XACT 3-axis attitude determination and control system," *Journal of Small Satellites*, vol. 6, no. 3, pp. 651–662, 2017.
[10] W. W. Weiss *et al.*, "BRITE-constellation: Nanosatellites for precision photometry of bright stars," *Publications of the Astronomical Society of the Pacific*, vol. 126, no. 940, pp. 573–585, jun 2014.
[11] Y. Koyama *et al.*, "SOTA: Small Optical Transponder for micro-satellite," in *2011 International Conference on Space Optical Systems and Applications (ICSOS)*. IEEE, may 2011.
[12] A. Carrasco-Casado *et al.*, "LEO-to-ground optical communications using SOTA (Small Optical TrAnsponder) – Payload verification results and experiments on space quantum communications," *Acta Astronautica*, vol. 139, pp. 377–384, oct 2017.
[13] S. Janson *et al.*, "The NASA Optical Communication and Senor Demonstration program: initial flight results," in *29th Annual AIAA/USU Conference on Small Satellites*, 2016.
[14] T. S. Rose *et al.*, "Optical communications downlink from a 1.5u cubesat: OCSD program (conference presentation)," in *Free-Space Laser Communications XXXI*, H. Hemmati *et al.*, Eds. SPIE, mar 2019.
[15] O. Čierny *et al.*, "On-orbit beam pointing calibration for nanosatellite laser communications," *Optical Engineering*, vol. 58, no. 04, p. 1, nov 2018.
[16] C. Fuchs *et al.*, "Update on DLR's OSIRIS program and first results of OSIRISv1 on Flying Laptop," in *Proc. of SPIE*, vol. 10910, 2019.
[17] M. Storm *et al.*, "Cubesat laser communications transceiver for multi-Gbps downlink," in *31st Annual AIAA/USU Conference on Small Satellites*, 2017.
[18] Hyperion Technologies. [Online]. Available: https://hyperiontechnologies.nl/products/cubecat/?cn-reloaded=1

[19] NASA. (2018, Dec.) State of the Art of Small Spacecraft Technology - Guidance, Navigation and Control. [Online]. Available: https://sst-soa.arc.nasa.gov/05-guidance-navigation-and-control
[20] C. Payne *et al.*, "Integration and testing of the nanosatellite optical downlink experiment," in *32nd Annual AIAA/USU Conference on Small Satellites*, 2018.
[21] P. Serra *et al.*, "Optical communications crosslink payload prototype development for the Cubesat Laser Infrared CrosslinK (CLICK) mission," in *33rd Annual AIAA/USU Conference on Small Satellites*, 2019.
[22] F. Sansone *et al.*, "Compact stabilized pointing system," WO Patent WO2 017 115 204A1, 2017.
[23] J. P. Merlet, "Direct kinematics of parallel manipulators," *IEEE Transactions on Robotics and Automation*, vol. 9, no. 6, pp. 842–846, Dec 1993.
[24] P. Nanua *et al.*, "Direct kinematic solution of a Stewart platform," *IEEE Transactions on Robotics and Automation*, vol. 6, no. 4, pp. 438–444, Aug 1990.
[25] M. Kobayashi *et al.*, "Track seek control for hard disk dual-stage servo systems," *IEEE Transactions on Magnetics*, vol. 37, no. 2, pp. 949–954, Mar 2001.
[26] R. Horowitz *et al.*, "Dual-stage servo systems and vibration compensation in computer hard disk drives," *Control Engineering Practice*, vol. 15, no. 3, pp. 291 – 305, 2007, selected Papers Presented at the Third IFAC Symposium on Mechatronic Systems (2004).
[27] G. F. Franklin *et al.*, *Digital Control of Dynamic Systems*, 3rd ed. Boston, MA, USA: Addison-Wesley Longman Publishing Co., Inc., 1997.
[28] G. Franklin *et al.*, *Feedback Control of Dynamic Systems, Global Edition*. Pearson Education Limited, 2015.
[29] F. Sansone *et al.*, "A miniature stabilized platform for lasercom terminals on-board nanosatellites," in *64th International Astronautical Congress*, vol. 10, 2013.
[30] F. Sansone, "Technologies for a miniature LEO satellites telecommunication network," Ph.D. dissertation, University of Padova, Italy, 2015.
[31] K. J. Åström *et al.*, *Computer-controlled Systems (3rd Ed.)*. Upper Saddle River, NJ, USA: Prentice-Hall, Inc., 1997.

Riccardo Antonello (M '02) received the Laurea Degree in Computer Engineering in 2002 and the Ph.D. in Automatic Control in 2006 from the University of Padova, Italy. He has been a Research Associate at the Dept. of Mechanical and Structural Engineering, University of Trento, Italy, from 2006 to 2010, and then at the Dept. of Management and Engineering, University of Padova, Italy, from 2010 to 2015. Since 2015, he joined the Dept. of Information Engineering, University of Padova, Italy, as a Laboratory Assistant. His research interests lie in the areas of control systems, real-time embedded systems, electric drives and mechatronics.

Francesco Branz is a researcher at the Dept. of Information Engineering and a lecturer in Attitude Control of Satellites at Dept. of Industrial Engineering, University of Padova, Italy. He received his Ph.D. in 2016 at the Center of Studies and Activities for Space "G. Colombo" with a thesis on modelling and control of dielectric elastomer actuators for space robotics. His research also focuses on CubeSat technologies for attitude simulation and control, close range relative navigation and docking systems. He is participating to the development of LaserCube as an external contractor at Stellar Project.

Francesco Sansone is system engineer at Stellar Project. He has a Ph.D. in Space Science and Technology from the Centre of Studies and Activities for Space (CISAS) "G. Colombo" of the University of Padova. His research and professional activities are in the field of systems and technologies for enhancing the capabilities of nanosatellites. This includes laser communication and relative navigation systems. He participated to and supported several research and student projects testing critical technologies in low-gravity environment. Francesco is co-inventor of the LaserCube stabilisation and pointing subsystem and lead engineer for the development of the LaserCube terminal.

Angelo Cenedese received the M.S. (1999) and the Ph.D. (2004) degrees from the University of Padova, Italy, where he is currently an Associate Professor with the Department of Information Engineering and leader of the SPARCS (SPace and AeRial Control Systems) research group. He has held several visiting positions at the UKAEA-JET laboratories in the Culham Research Centre (UK), the UCLA Vision Lab (CA-USA), the F4E European Agency (Spain). His research interests include system modeling, control theory and its applications, sensor and actuator networks, multi agent systems. On these subjects, he has published more than 150 papers and holds three patents.

Alessandro Francesconi is associate professor of Space Systems at University of Padova. His main research topics are related to spacecraft systems and miniature satellites (with focus on on-orbit servicing, docking and capture of non-cooperative spacecraft, and laser communication), and space debris (where he has 20+ years of experience in studying hypervelocity impacts, satellites collisions and fragmentation). He has been chairman of the Protection Working Group of the Inter Agency Debris Coordination Committee, and he is member of the IAA Permanent Committee on Space Debris. He is co-founder of Stellar Project and co-inventor of the LaserCube stabilisation and pointing subsystem.